

Periodic orbits and gravitational waveforms of spinning particles in nonlocal Gravity

Moisés Bravo-Gaete,^a Jianhui Lin,^b Yunlong Liu,^c Xiangdong Zhang^b

^aDepartamento de Matemática, Física y Estadística, Facultad de Ciencias Básicas, Universidad Católica del Maule, Casilla 617, Talca, Chile.

^bDepartment of Physics, South China University of Technology, Guangzhou 510641, China.

^cSchool of Science, Kunming University of Science and Technology, Kunming 650093, China.

E-mail: mbravo@ucm.cl, 202510188472@mail.scut.edu.cn, phliuyunlong@kust.edu.cn, scxdzhang@scut.edu.cn

Abstract. In this paper, we investigate the dynamics and gravitational-wave signatures of periodic orbits of spinning test particles moving in the equatorial plane around static, spherically symmetric black holes within the framework of Deser-Woodard nonlocal gravity. Based on the Mathisson-Papapetrou-Dixon equations, combined with the Tulczyjew spin supplementary condition, we derive the orbital dynamic equations for spinning particles moving in the equatorial plane and impose a timelike constraint to exclude unphysical superluminal trajectories. By comparing with the classical Schwarzschild black hole, we systematically analyze the effects of the nonlocal gravitational parameters ζ and b on the effective potential governing the radial motion of particles and the innermost stable circular orbit. In addition, gravitational waveforms exhibit significant phase differences: an increase in ζ induces a phase delay, whereas an increase in b results in a phase advance. A one-year simulation of the orbital evolution of an extreme mass ratio inspiral demonstrates that when $b = 2$ and $\zeta \approx 10^{-6}$, the mismatch between the gravitational waveforms predicted for the nonlocal gravity black hole and those for the Schwarzschild black hole reaches the distinguishable threshold ($\mathcal{M} = 0.0125$), providing a basis for observational discrimination between general relativity and nonlocal gravity.

Keywords: nonlocal gravity, spinning test particles, periodic orbits, gravitational waveforms

Contents

1	Introduction	1
2	The equation of motion of spinning particles	2
2.1	Black hole solutions in NLG	2
2.2	Equation of motion of spinning particles	3
2.3	Timelike condition of the orbits	5
3	Effective potential and ISCO	6
3.1	Effective potential	6
3.2	ISCO	8
4	Periodic orbits and gravitational waves	9
4.1	Periodic orbits	9
4.2	Gravitational waveforms from period orbits	12
4.3	Numerical results	15
5	Conclusion and discussion	16

1 Introduction

At the classical level, general relativity (GR) has been observationally validated as the most successful theory of gravity to date. Nevertheless, it encounters unresolved issues in the more extreme infrared and ultraviolet regimes. On one hand, the standard cosmological model introduces the cosmological constant Λ to give an effective description of cosmic acceleration, interpreting Λ as dark energy with negative pressure[1–4]. However, the observed value of the vacuum energy density associated with Λ differs from theoretical predictions in quantum field theory (QFT) by an enormous order of magnitude [5, 6], a discrepancy known as the fine-tuning problem. On the other hand, singularities in the universe and black holes imply a need to quantize gravity, yet applying traditional perturbative QFT methods to gravity leads to non-renormalizable divergences. All of these challenges indicate that our understanding of gravitational interactions remains incomplete, providing compelling motivation to develop a gravitational theory that is self-consistent across all scales.

As a prominent class of modified gravity theories, nonlocal gravity (NLG) has made notable progress in addressing the core challenges facing classical GR. In contrast to traditional local gravity, NLG theories are characterized by effective actions that incorporate various forms of nonlocal operators, aiming to integrate the intrinsic non-locality of quantum systems into gravitational interactions. NLG theories are broadly divided into integral-kernel gravity and infinite-derivative gravity [7].

When it comes to cosmic acceleration, integral kernel gravity introduces non-locality via the inverse d'Alembert operator [8–16]. It can naturally explain late-time cosmic expansion without invoking a cosmological constant, serving as an alternative to dark energy, but its higher-order nonlinear nature poses challenges for solving equations.

In addition, infinite-derivative gravity incorporates a transcendental analytic entire function of the d'Alembert operator into the action [17–22]. When expanded, this yields an infinite series of higher-derivative terms—directly encoding non-locality. This framework satisfies

both renormalizability and unitarity, and regularizes curvature singularities in black holes and cosmology, thereby addressing the incompleteness of classical spacetime [18, 19].

Nevertheless, despite these significant advances, a fully consistent quantum theory of gravity that remains self-consistent across both the ultraviolet and infrared regimes has yet to be realized. Among these NLG theories, the Deser–Woodard (DW) model—a prominent representative of integral-kernel gravity—naturally incorporates a delayed response to the transition from radiation to matter dominance in cosmology and avoids fine-tuning [8]. However, this model was later criticized for lacking a viable screening mechanism to suppress small-scale nonlocal effects, rendering it inconsistent with lunar laser ranging tests [23]. Subsequently, an improved variant of the model was proposed [14], and quasinormal mode analyses of black holes within this framework have been performed [24]. Recently, by employing an appropriate tetrad formalism, new nonlocal static spherically symmetric black hole [25] and wormhole solutions [26] have been constructed, and the quasinormal modes for the black hole solution are presented in [27].

The strong gravitational field near black holes provides a natural laboratory for testing various theories of gravity. In this work, we focus on the black hole solutions of DW NLG model [25], and we aim to uncover the spacetime structure near the black hole within this theoretical framework by analyzing the orbital dynamics of particles in its vicinity. Here, the parameters characterizing these solutions directly determine the geometry and therefore leave imprints on characteristic observational effects, providing a crucial basis for distinguishing this class of NLG black hole solutions. In particular, gravitational waves (GWs) from the inspiral and merger of compact objects are crucial probes of strong-field gravity, with their waveforms closely linked to the intrinsic properties of the emitting sources [28–30]. Most compact objects in the universe possess intrinsic spin, and spin-curvature coupling in their orbital dynamics significantly modulates the innermost stable circular orbit (ISCO) [31–34] and shapes the GW waveform, rendering spinning compact objects essential for building precise theoretical GW templates. Furthermore, Extreme Mass Ratio Inspirals (EMRIs) are powerful tools for detecting GWs [35, 36]. Studying EMRI dynamics on this nonlocal gravity background, therefore, will provide critical theoretical support for future gravitational wave observations to test NLG theories and identify black hole solutions.

The structure of this paper is organized as follows. In Section 2, we briefly review black hole solutions in NLG and present the equations of motion for spinning particles together with the timelike condition for their orbits. In Section 3, we further analyze the effective potential that governs radial motion, determine the ranges of energy and angular momentum parameters that correspond to bound orbits, and compute the innermost stable circular orbit (ISCO). Section 4 is devoted to the classification of periodic orbits, the calculation of gravitational waveforms, and the presentation of our numerical results. Finally, in Section 5, we summarize our main findings and outline directions for future research.

2 The equation of motion of spinning particles

2.1 Black hole solutions in NLG

In this subsection, we begin by providing a brief review of the Deser–Woodard NLG model [14]. A class of static, spherically symmetric black hole solutions to the vacuum field equations of NLG was obtained perturbatively in [25], whose line element, expressed in the coordinates

(t, r, θ, ϕ) , can be written as:

$$ds^2 = -f(r) dt^2 + \frac{1}{h(r)} dr^2 + g(r)(d\theta^2 + \sin^2 \theta d\phi^2) \quad (2.1)$$

with

$$f(r) = 1 - \frac{2}{r} - \frac{\zeta}{r^b}, \quad (2.2)$$

$$h(r) = 1 - \frac{2}{r} + \frac{\zeta}{3^b r^{b+1} (r-3)^2} \left\{ 3^b r [b(r-3)(r-2) + 4r - 9] - 3(r-2)(2r-3)r^b \right\}, \quad (2.3)$$

$$g(r) = r^2. \quad (2.4)$$

For convenience, and without loss of generality, we set the black hole mass to unity ($M = 1$), while the real parameters satisfy $0 < \zeta \ll 1$ and $b > 1$. The parameter ζ controls the magnitude of the nonlocal deviation from the Schwarzschild geometry: when $\zeta = 0$, the solution reduces to the classical Schwarzschild black hole. This metric satisfies the asymptotic flatness condition, and one can verify that an expansion near the Schwarzschild horizon shows that the event horizon r_H is located at

$$r_H = 2 + \frac{\zeta}{2^{b-1}},$$

to leading order in the perturbative parameter ζ . Apart from the essential singularity at the center, no additional singularities arise outside the horizon.

In addition, to prevent any misunderstanding, it must be emphasized once again that the line element (2.1)-(2.4) represents a class of phenomenological solutions. Different values of ζ and b do not merely represent adjustable parameters of a single theory but correspond to distinct realizations of nonlocal gravitational models. Therefore, in all subsequent discussions concerning the parameters ζ and b , it is imperative to clearly recognize that this is a comparative study of a category of NLG theories.

2.2 Equation of motion of spinning particles

It is well known that in curved spacetime, the motion of the simplest point-like particle (in the monopole approximation) is described by the geodesic equation. However, a spinning particle in general does not follow a geodesic due to its spin couples to the spacetime curvature. In Refs. [37–39], the authors systematically derived the equations of motion for a spinning particle in curved spacetime under the pole–dipole approximation, i.e., the so-called Mathisson–Papapetrou–Dixon (MPD) equations,

$$\frac{DP^a}{D\tau} = -\frac{1}{2} R^a_{bcd} v^b S^{cd}, \quad (2.5)$$

$$\frac{DS^{ab}}{D\tau} = P^a v^b - P^b v^a. \quad (2.6)$$

Here, $D/D\tau$ denotes the covariant derivative with respect to the affine parameter τ along the world line, R^a_{bcd} the Riemann tensor, P^a the four-momentum, $v^a = dx^a/d\tau$ the four-velocity, and S^{ab} is the antisymmetric spin tensor. It is worth noting that the above Eqs. (2.5) and

(2.6) do not uniquely determine all the information about the spinning particle, since the center of mass of the particle has not yet been fixed. Therefore, we need to introduce the Tulczyjew spin supplementary condition:

$$P_a S^{ab} = 0, \quad (2.7)$$

which are allowed to determine the remaining degrees of freedom. The choice of supplementary condition is not unique; see [40] for a detailed discussion.

Combining Eqs. (2.5)- (2.7), we can obtain two conserved quantities associated with mass m and spin \mathcal{S} along the trajectory

$$P^a P_a = -m^2, \quad (2.8)$$

$$\mathcal{S}^2 = \frac{1}{2} S^{ab} S_{ab}. \quad (2.9)$$

Following the convention adopted in [41], we normalize the orbital affine parameter τ as

$$P^a v_a = -m. \quad (2.10)$$

With this choice, the four-vector v^a does not coincide with the normalized four-velocity and, in general, does not satisfy the normalization condition $v^a v_a = -1$. To facilitate subsequent calculations, we introduce the spin four-vector [40]

$$S^a = -\frac{1}{2m} \epsilon^a_{bcd} P^b S^{cd}, \quad (2.11)$$

where ϵ^a_{bcd} is the Levi-Civita tensor, and the spin four-vector is constrained by

$$S^a S_a = \mathcal{S}^2. \quad (2.12)$$

For simplicity, in this paper we restrict ourselves to trajectories lying in the equatorial plane ($\theta = \pi/2$). It follows immediately that $P^\theta = 0$ and $S^{b\theta} = 0$. Furthermore, substituting P^θ and $S^{b\theta}$ into Eq. (2.11), and using Eq. (2.12), we can identify

$$S_t = S_r = S_\phi = 0, \quad S_\theta = -\mathcal{S}\sqrt{g}. \quad (2.13)$$

To simplify the notation, we shorten $g(r)$ to g (it should be noted that g does not represent the determinant of the metric). In subsequent sections, f and h will also denote the expressions given in Eqs. (2.2) and (2.3). Here \mathcal{S} not only characterizes the magnitude of the spin, but also encodes its orientation: for $\mathcal{S} > 0$ the particle spin is aligned with the orbital angular momentum, whereas for $\mathcal{S} < 0$ it is anti-aligned. An equivalent form of the spin tensor (2.11) reads [40]:

$$S^{ab} = -\frac{1}{m} \epsilon^{abcd} S_c P_d, \quad (2.14)$$

from which one can obtain the nonvanishing components

$$S^{tr} = -\frac{\mathcal{S} P_\phi}{m} \sqrt{\frac{h}{fg}}, \quad (2.15)$$

$$S^{t\phi} = \frac{\mathcal{S} P_r}{m} \sqrt{\frac{h}{fg}}, \quad (2.16)$$

$$S^{r\phi} = -\frac{\mathcal{S} P_t}{m} \sqrt{\frac{h}{fg}}. \quad (2.17)$$

A Killing vector ξ^a that describes spacetime symmetry can be associated with a conserved quantity [42]

$$C = \xi^a P_a + \frac{1}{2} S^{ab} \nabla_a \xi_b. \quad (2.18)$$

In a static, spherically symmetric spacetime, there are two Killing vectors: $(\partial/\partial t)^a$ and $(\partial/\partial\phi)^a$, which are associated with the energy of the spinning particle and the total angular momentum, respectively,

$$\mathcal{E} = -P_t + \frac{\mathcal{S}P_\phi f'}{2m} \sqrt{\frac{h}{fg}}, \quad (2.19)$$

$$\mathcal{J} = P_\phi - \frac{\mathcal{S}P_t g'}{2m} \sqrt{\frac{h}{fg}}. \quad (2.20)$$

Using these conserved quantities, together with the normalization condition (2.8), the components of the four-momentum can be expressed as:

$$P_t = \frac{-4mEfg + 2msJf'\sqrt{fhg}}{4fg - s^2h f' g'}, \quad (2.21)$$

$$P_\phi = \frac{4mJfg - 2msEg'\sqrt{fhg}}{4fg - s^2h f' g'}, \quad (2.22)$$

$$P_r^2 = -g_{rr} \left(g^{tt} P_t^2 + g^{\phi\phi} P_\phi^2 + m^2 \right), \quad (2.23)$$

where $E = \mathcal{E}/m$, $J = \mathcal{J}/m$ and $s = \mathcal{S}/m$ denote the energy, angular momentum, and spin per unit mass of the particle, respectively.

So far, we have successfully completed the detailed calculation of the four-momentum. The four-velocity most directly related to the orbit can be obtained from [41]

$$v^a = \frac{P^a}{m} + \frac{2S^{ab}R_{bcde}P^cS^{de}}{m(4m^2 + R_{ijkl}S^{ij}S^{kl})}. \quad (2.24)$$

Its derivation is not particularly straightforward and is somewhat tedious, details can be found in [43].

2.3 Timelike condition of the orbits

It follows from Eq. (2.6) that the directions of the four-momentum and four-velocity are generally inconsistent, which is essentially caused by the spin-gravity coupling effect. While Eq. (2.8) ensures the timelike property of the four-momentum, the affine parameter selected in Eq. (2.10) implies that the normalization condition of the four-velocity does not hold. Therefore, certain parameter ranges can cause the velocity of the particle to exceed the speed of light and its trajectory to become spacelike, which is physically unacceptable. To exclude such non-physical results, we introduce a superluminal constraint

$$v^a v_a < 0, \quad (2.25)$$

which is taken into account in all subsequent practical calculations.

3 Effective potential and ISCO

3.1 Effective potential

Since we focus on bound and (marginally) stable circular motion in the vicinity of a black hole, the spinning particles considered here neither escape to infinity nor plunge into the horizon. We restrict the motion to the equatorial plane. To identify the boundaries of its radial motion, the most straightforward approach would be to analyze the locations where $v^r = 0$. However, a more convenient approach follows from the structure of Eq. (2.24). A detailed evaluation shows that

$$v^r = U(r)P^r.$$

Because the function $U(r)$ is nonvanishing outside the event horizon for the parameter ranges of interest, the turning points of the trajectory are equivalently determined by the condition $P^r = 0$. Directly from Eq. (2.23), we have:

$$\begin{aligned} \frac{(P^r)^2}{m^2} &= \frac{(\mathcal{A}E^2 + \mathcal{B}E + \mathcal{C})}{\mathcal{D}} \\ &= \frac{1}{\mathcal{D}} \left[E - \left(\frac{-\mathcal{B} + \sqrt{\mathcal{B}^2 - 4\mathcal{A}\mathcal{C}}}{2\mathcal{A}} \right) \right] \\ &\quad \times \left[E - \left(\frac{-\mathcal{B} - \sqrt{\mathcal{B}^2 - 4\mathcal{A}\mathcal{C}}}{2\mathcal{A}} \right) \right], \end{aligned} \quad (3.1)$$

where

$$\mathcal{A} = 4fh(4g^2 - s^2hg'^2), \quad (3.2)$$

$$\mathcal{B} = 16sJh^{3/2}\sqrt{fg}(fg' - gf'), \quad (3.3)$$

$$\mathcal{C} = h[4J^2g(s^2hf'^2 - 4f^2) - (s^2hf'g' - 4fg)^2], \quad (3.4)$$

$$\mathcal{D} = (s^2hf'g' - 4fg)^2. \quad (3.5)$$

Note that \mathcal{D} is manifestly nonnegative, guaranteeing regular behavior of the radial equation away from singular points. The effective potential of relevance thus is defined as

$$V_{\text{eff}} = \frac{-\mathcal{B} + \sqrt{\mathcal{B}^2 - 4\mathcal{A}\mathcal{C}}}{2\mathcal{A}}, \quad (3.6)$$

where the positive square root is chosen to correspond to a future-directed orientation. Bound motion requires the discriminant $\mathcal{B}^2 - 4\mathcal{A}\mathcal{C} \geq 0$, ensuring that the effective potential remains real. It follows directly that when the particle's energy E is equal to the effective potential, this marks the turning point of its radial motion. We introduce the orbital angular momentum parameter $l = J - s$, which subtracts the intrinsic spin contribution s from the conserved total angular momentum J .

As illustrated in Fig. 1, with appropriate parameter choices, we clearly observe that a potential barrier (corresponding to a local maximum) emerges in the effective potential near the horizon, and $V_{\text{eff}} \rightarrow 1$ as $r \rightarrow +\infty$, this asymptotic limit follows from the Schwarzschild normalization at spatial infinity. If the particle's energy exceeds one, it will escape to infinity, corresponding to an unbound orbit. Similarly, if the local maximum (of the potential barrier) is less than one and the particle's energy surpasses this barrier, the particle will eventually

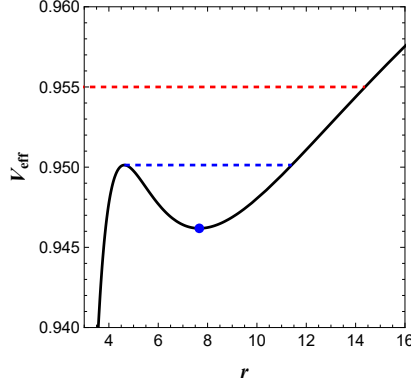


Figure 1: Effective potential V_{eff} as a function of r with $b = 2, \zeta = 0.2, s = 0.3, l = 3.5$. The local maximum (blue dashed curve) defines the potential barrier separating bound and plunging trajectories, while the local minimum (blue dots) corresponds to stable circular orbits.

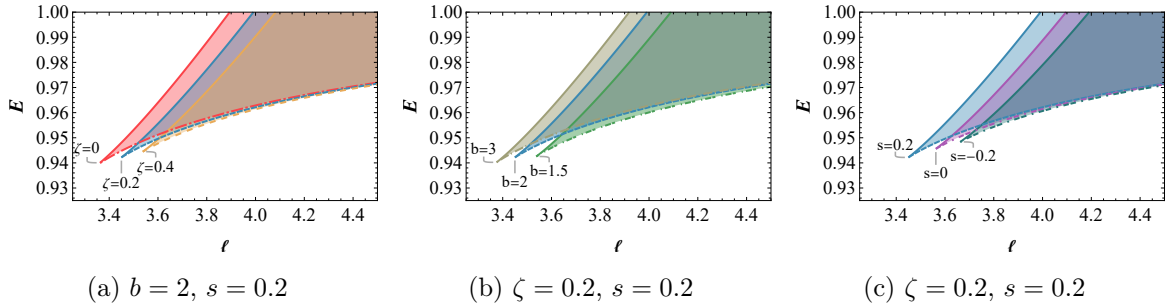


Figure 2: Allowed parameter region in the (E, l) plane for bound motion. The shaded area corresponds to energies lying between the local maximum and minimum of the effective potential. The vertex of the shaded region marks the ISCO, where the two extrema merge.

fall into the black hole, which corresponds to the red dashed line in Fig. 1. Neither of these scenarios is desirable. For fixed parameters, the appropriate energy range for the particle is $E_{\text{min}} < E < E_{\text{max}}$, where E_{min} denotes the local maximum at the potential barrier and E_{max} denotes the local minimum of V_{eff} .

Fig. 2 provides an intuitive illustration in which the shaded region denotes the parameter range within which bound orbits can exist. For a fixed angular momentum, the upper energy bound decreases as ζ increases. In contrast, increasing b causes the entire parameter range to shift to the left, with the upper bound of E instead increasing. Furthermore, the particle can carry higher energy when its spin is aligned with the orbital angular momentum.

To further clarify the influence of the model parameters, Fig. (3) shows the variation of the effective potential with r for different parameter values. Here, as before, $l = J - s$ denotes the orbital angular momentum. In Fig. (3a), increasing ζ causes the effective potential to decrease, whereas Fig. (3b) shows that the effective potential tends to rise with an increasing b . These trends indicate that stronger NLG correction terms result in a lower potential barrier. In Fig. (3c), as the spin s varies from -0.5 to 0.5 , the effective potential also increases steadily, which demonstrates that spin can alter the stability of the particle's orbit. In each panel, the blue dashed line corresponds to the cases where the maximum and minimum of the effective

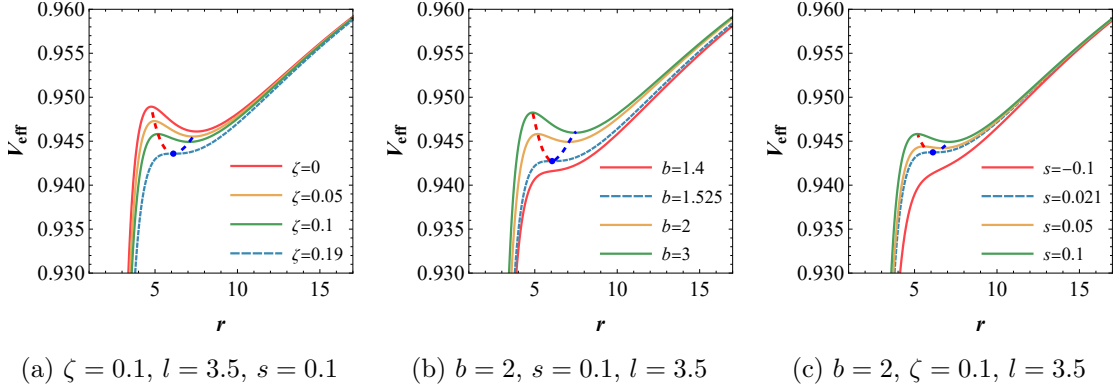


Figure 3: The variation of V_{eff} with respect to the radial coordinate r . (a) Distinct b for fixed ζ, l and s ; (b) Distinct ζ for fixed b , s and l ; (c) Distinct positive s for fixed l , b and ζ . The red dashed line traces the maxima (peaks) of the effective potential curves, while the dark blue dashed line marks the minima (valleys) across parameter variations.

potential V_{eff} coincide. Meanwhile, the dark blue solid points actually mark the ISCO, which will be introduced in the next subsection.

3.2 ISCO

Here, we focus on the properties of ISCO. Its definition can be expressed via the conditions:

$$V_{\text{eff}}(r) = E, \quad \frac{dV_{\text{eff}}(r)}{dr} = 0, \quad \frac{d^2V_{\text{eff}}}{dr^2} = 0, \quad (3.7)$$

which correspond to a circular orbit at the inflection point of the effective potential. Despite its name as the “innermost stable circular orbit”, the mathematical conditions—with both the first and second derivatives of the effective potential vanishing—mean the orbit is actually unstable. When a particle on this orbit experiences small perturbations, it can hardly sustain circular motion and will eventually plunge into the black hole. However, we use this terminology to align with other papers.

These three Eqs. (3.7) allow us to solve for $\{r_{\text{ISCO}}, E_{\text{ISCO}}, l_{\text{ISCO}}\}$, provided the remaining nonlocal gravitational parameters are fixed. In Fig. 4, we display the ISCO properties for different ζ values. For co-rotating particles ($sl > 0$), increasing spin s reduces the ISCO radius, energy, and angular momentum. In contrast, for a fixed spin s , larger values of ζ leads to an increase in the ISCO radius, energy, and angular momentum. For counter-rotating particles ($sl < 0$), the trend of the ISCO energy is exactly opposite to that of co-rotating particles: an increase in ζ leads to a decrease in the ISCO energy.

Fig. 5 illustrates the ISCO properties across different values of the parameter b . Increasing the spin s again decreases the ISCO in radius, energy, and angular momentum, consistent with previous analysis. For a fixed s , larger values of b lead to a smaller ISCO radius, energy and angular momentum. Additionally, the vertex of the shaded region in Fig. 2 corresponds precisely to the ISCO values of energy and angular momentum, and its variation trends across different values of ζ , b , and s align with the analysis presented here.

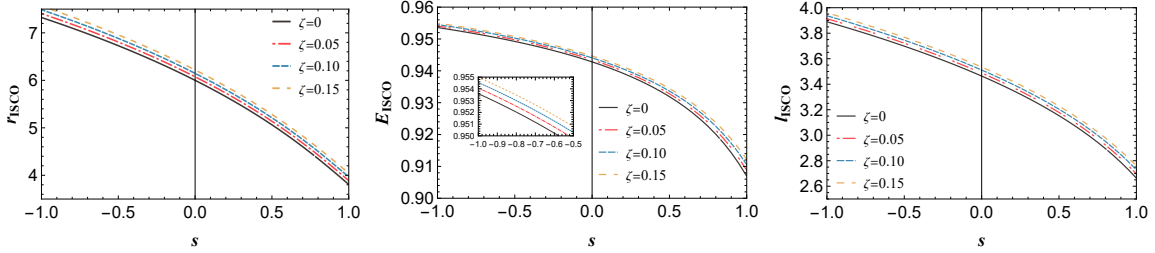


Figure 4: Dependence of the ISCO radius (left), energy (center), and orbital angular momentum (right) on the spin parameter s , for several values of the parameter ζ , with $b = 2$ fixed. Co-rotating ($sl > 0$) and counter-rotating ($sl < 0$) configurations exhibit distinct trends, illustrating how nonlocal corrections modify spin-orbit coupling and shift the ISCO location.

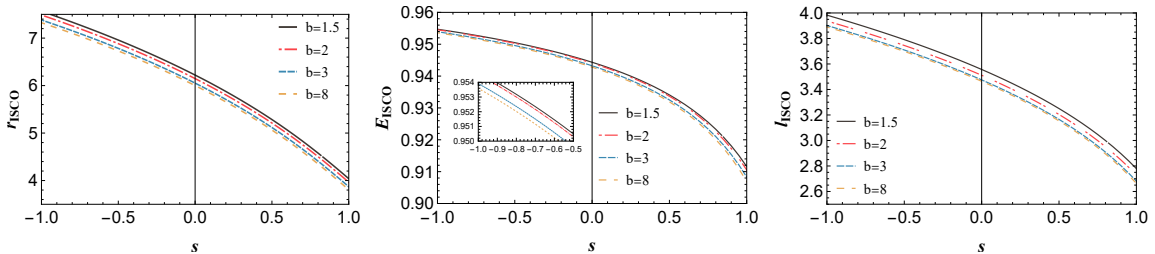


Figure 5: ISCO radius (left), energy (center), and orbital angular momentum (right) as functions of the spin parameter s for different values of b , with $\zeta = 0.1$ fixed. Increasing b shifts the ISCO inward and lowers the corresponding energy, reflecting the influence of the nonlocal parameter on the near-horizon geometry.

4 Periodic orbits and gravitational waves

Periodic orbits represent a special category of bound orbits, which are not only easier to handle but also serve as the reference base, such that any arbitrary orbit can be treated as a small perturbation of a precisely defined periodic orbit [44]. As such, the study of periodic orbits allows us to capture the key physical characteristics. Furthermore, discrepancies in spacetime geometry predicted by different gravitational theories are directly imprinted in the features of gravitational waveforms. This offers a powerful observational tool for testing and constraining various gravitational theories. In this section, we first present a brief introduction to periodic orbits and GWs, followed by a collective presentation of the numerical calculation results.

4.1 Periodic orbits

We adopt the classification scheme for periodic orbits introduced in [44] to examine whether NLG black holes can be distinctly differentiated from their Schwarzschild counterparts. The periodic motion of particles in the equatorial plane can be characterized by three integers, namely (z, w, v) :

z (zoom): the number of "leaves" formed by each periodic orbit before closure;

w (whirl): the number of additional circumferential revolutions executed by a particle near the perihelion during a single radial period (from one aphelion to the perihelion and

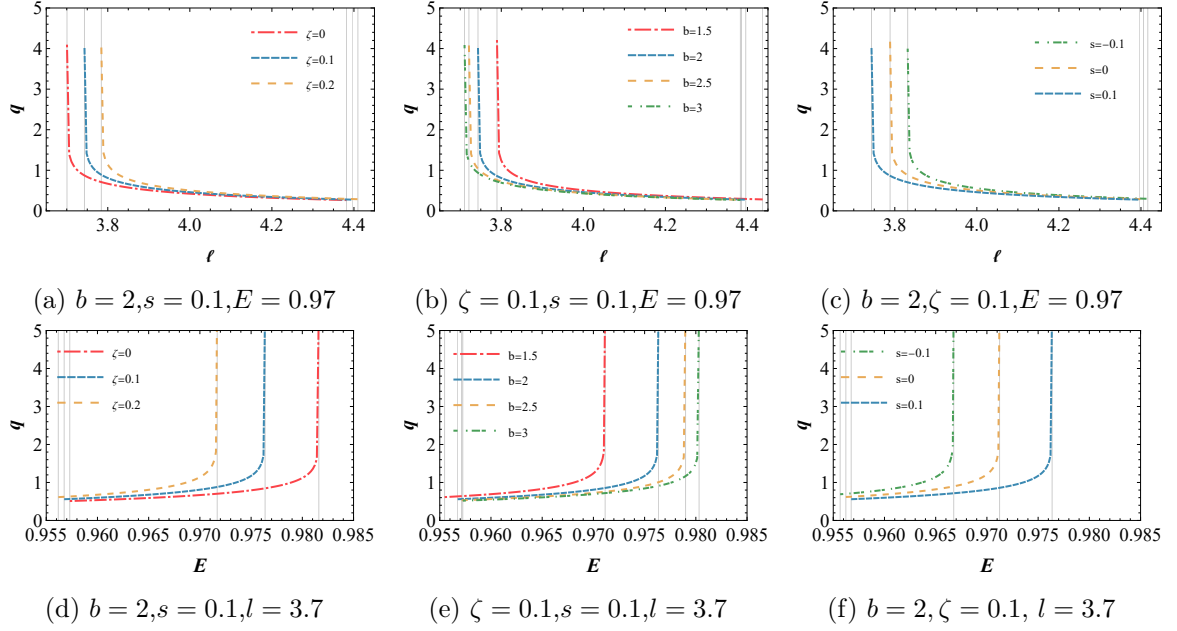


Figure 6: Upper panels: Dependence of the parameter q and the orbital angular momentum l for different values of: (a) ζ ; (b) b ; (c) s . **Lower panels:** Dependence of the parameter q and the Energy E under the same parameter variations: (d) varying ζ ; (e) varying b ; (f) varying s .

then to the next aphelion);

v (vertex): the number of vertices skipped by the particle when moving from the first aphelion to the next. For orbits with $z \geq 2$, there exist multiple aphelia that make up the vertices of a polygon. These vertices are numbered sequentially in the direction of orbital rotation. For example, the initial aphelion is denoted as $v = 0$; $v = 1$ means that the particle travels directly from the initial aphelion to the first vertex, while $v = 2$ implies that the particle moves from the initial aphelion to the second vertex, and so forth.

Notably, the zoom-whirl behavior is a physically realizable orbital feature that modulates gravitational waveforms even with gravitational radiation dissipation [45]. The integers (z, w, v) can be related to a rational number q , which satisfies the following relation for periodic orbits [44]

$$q = \frac{\Delta\phi}{2\pi} - 1 = w + \frac{v}{z}. \quad (4.1)$$

Here, $\Delta\phi$ denotes the azimuthal angle traversed by the particle over a complete radial period. It can be derived by integrating the relation between azimuthal and radial motion, which reads:

$$\Delta\phi = 2 \int_{r_1}^{r_2} \left(\frac{d\phi}{dr} \right) dr, \quad (4.2)$$

where r_1 and r_2 denote the perihelion and aphelion, respectively. Using Eq. (2.24), we have

$$\frac{d\phi}{dr} = \frac{d\phi}{d\tau} \frac{d\tau}{dr} = \frac{v^\phi}{v^r}, \quad (4.3)$$

which depends on the energy E , orbital angular momentum l , spin s , as well as ζ and b . By combining Eqs. (4.1)-(4.3), once the values of s , ζ and b are specified, the correlation relationships between q and E , l can be derived separately.

Detailed calculations are presented in Fig. 6. In the upper panels, with E kept constant, q increases gradually and eventually diverges as l decreases. In the lower panels, with l fixed, q rises slowly and diverges as E approaches its maximum value. Moreover, for a fixed value of q , an increase in ζ leads to a larger orbital angular momentum but a smaller energy. In contrast, a larger b results in a smaller orbital angular momentum but a larger energy, showing a competitive trend against the effect of ζ . When the spin is aligned with the orbital angular momentum, the minimum value of l decreases while the maximum value of E increases. These expanded parameter ranges indirectly imply that co-rotating particles are more likely to form periodic orbits—meaning that they tend to stabilize the orbit. Conversely, particles with spin anti-aligned with the orbital angular momentum reduce orbital stability. These trends are consistent with those discussed in Figs. 2 and 3, and such characteristics can serve as a basis for distinguishing between different NLG black holes.

The calculation of specific orbits depends on Eq. (2.24). This relationship depends explicitly on r but implicitly on τ (i.e., $v^a(r(\tau))$). The system of differential equations for the trajectory is given as follows

$$\begin{aligned} \frac{dt}{d\tau} &= v^t, \\ \frac{d^2r}{d\tau^2} &= \frac{dv^r}{dr} \cdot v^r, \\ \frac{d\theta}{d\tau} &= 0, \\ \frac{d\phi}{d\tau} &= v^\phi. \end{aligned} \tag{4.4}$$

Given the initial conditions, the orbit parameterized by the affine parameter τ can be derived. However, for the convenience of subsequent GW calculations, we aim here to use the particle's coordinate time t instead of τ as the parameter along its trajectory. The transformed system reads:

$$\begin{aligned} r''(t) &= \frac{d^2r}{d\tau^2} \cdot \left(\frac{d\tau}{dt} \right)^2 + \frac{dr}{d\tau} \cdot \frac{d^2\tau}{dt^2} \\ &= \frac{v^r}{(v^t)^2} \cdot \frac{dv^r}{dr} - \frac{(r'(t))^2}{v^t} \cdot \frac{dv^t}{dr}, \\ \theta'(t) &= 0, \\ \phi'(t) &= \frac{d\phi}{d\tau} \cdot \frac{d\tau}{dt} = \frac{v^\phi}{v^t}, \end{aligned} \tag{4.5}$$

where the prime denotes differentiation with respect to t . The initial conditions are chosen as

$$r'(0) = 0, \quad r(0) = r_2, \quad \theta(0) = \pi/2, \quad \phi(0) = 0, \tag{4.6}$$

The functions $r(t)$ and $\phi(t)$ are obtained by numerically solving the above equations. Projecting these solutions onto the two-dimensional plane via $x = r(t) \cos \phi(t)$ and $y = r(t) \sin \phi(t)$ yields the trajectories of periodic orbits. We present our computational results together with the gravitational waveforms in Fig. 7 and discuss them in detail in Section 4.3.

4.2 Gravitational waveforms from period orbits

In realistic astrophysical scenarios, EMRIs consist of a compact object of much smaller mass orbiting a supermassive black hole. In this process, the compact object can be treated as a test particle, and the methods discussed in previous sections can be applied to some extent. In the present analysis, the system evolves sufficiently slowly, with negligible energy loss, so that the backreaction of gravitational radiation is neglected. In the subsequent discussion of GWs, we adopt the highly effective adiabatic approximation. Based on this assumption, we follow the numerical kludge approach described in [46] to compute the gravitational waveforms emitted by periodic orbits. While this is a phenomenological approach, empirically, as long as the orbital perihelion is not too close to the black hole, the numerically kludge waveforms rapidly generated by this method achieve extremely high overlap with the accurate Teukolsky-based waveforms [47].

First, we place the black hole at the coordinate origin and project the orbits in Boyer-Lindquist coordinates onto the Cartesian coordinates of a pseudo-flat spacetime

$$x_p = r \sin \theta \cos \phi, \quad y_p = r \sin \theta \sin \phi, \quad z_p = r \cos \theta. \quad (4.7)$$

Here, the subscript p denotes the Cartesian coordinates of the particle (i.e., (t_p, \vec{x}_p)), and t_p is in fact identified with the orbital time parameter t in Eqs. (4.5). This formulation facilitates the application of wave-generation formulas derived for flat spacetime. In the weak-field approximation, the metric can be decomposed as

$$g_{ab} = \eta_{ab} + h_{ab}, \quad (4.8)$$

with η_{ab} denoting the Minkowski metric and h_{ab} the metric perturbation. We may then define the trace-reversed metric perturbation as

$$\bar{h}^{ab} = h^{ab} - \frac{1}{2} \eta^{ab} h, \quad (4.9)$$

where $h = \eta^{cd} h_{cd}$ is the trace of h_{ab} . Upon imposing the Lorentz gauge condition $\partial_a \bar{h}^{ab} = 0$, we arrive at the linearized field equations:

$$\partial^c \partial_c \bar{h}^{ab} = -16\pi T^{ab}. \quad (4.10)$$

For a point particle moving along a trajectory, the energy-momentum tensor in flat spacetime can be written as

$$T^{ab} = m \cdot \frac{dx_p^a}{dt_p} \frac{dx_p^b}{dt_p} \delta^3(\vec{x} - \vec{x}_p), \quad (4.11)$$

In the slow-motion limit, GWs arise exclusively from the quadrupole moment contribution:

$$I^{ab}(t_p) = \int x^a x^b T^{00} d^3 x = m x_p^a x_p^b, \quad (4.12)$$

and the resulting waveform reads

$$\bar{h}^{ab}(t_{obs}, \vec{x}_{obs}) = \frac{2}{D} \frac{d^2 I^{ab}(t_p)}{dt_{obs}^2}, \quad (4.13)$$

with D the luminosity distance from the source to the observer. We denote the observer's position by $(t_{\text{obs}}, \vec{x}_{\text{obs}})$, and $t_{\text{obs}} = t_p + |\vec{x}_{\text{obs}} - \vec{x}_p|$ where the second term on the right-hand side accounts for the light-travel time between the particle and the observer. It is treated as a constant during the particle's motion. We now consider an observer located at the source's latitude and azimuthal angle (Θ, Φ) , and project \bar{h}^{ab} onto the spherical coordinates, with its non-vanishing components given by:

$$\begin{aligned} h^{\Theta\Theta} &= \cos^2 \Theta (\bar{h}^{xx} \cos^2 \Phi + h^{xy} \sin 2\Phi + \bar{h}^{yy} \sin^2 \Phi), \\ h^{\Phi\Theta} &= \cos \Theta \left(-\frac{1}{2} \bar{h}^{xx} \sin 2\Phi + \bar{h}^{xy} \cos 2\Phi + \frac{1}{2} \bar{h}^{yy} \sin 2\Phi \right), \\ h^{\Phi\Phi} &= \bar{h}^{xx} \sin^2 \Phi - \bar{h}^{xy} \sin 2\Phi + \bar{h}^{yy} \cos^2 \Phi. \end{aligned} \quad (4.14)$$

This derivation has taken into account the fact that $\bar{h}^{az} = 0$. In the standard transverse-traceless (TT) gauge, the observable gravitational waveform is written as

$$h_{TT}^{ab} = \frac{1}{2} \begin{pmatrix} 0 & 0 & 0 \\ 0 & h_+ & h_\times \\ 0 & h_\times & -h_+ \end{pmatrix} \quad (4.15)$$

where h_+ and h_\times are the two independent polarization states of GWs, with their explicit expressions given by

$$\begin{aligned} h_+ &= h^{\Theta\Theta} - h^{\Phi\Phi}, \\ h_\times &= 2h^{\Phi\Theta}. \end{aligned} \quad (4.16)$$

This set of operations achieves the matching of orbital parameters to gravitational waveforms.

To distinguish solutions of this class of nonlocal gravitational theories, it is also necessary to quantify the discrepancy between two gravitational waveforms. The overlap between two waveforms is characterized by introducing a noise-weighted inner product [48]:

$$\langle h_a | h_b \rangle = 2 \int_0^\infty \frac{h_a^*(f) h_b(f) + h_a(f) h_b^*(f)}{S_n(f)} df, \quad (4.17)$$

where $h_a(f)$ and $h_b(f)$ denote the frequency-domain representations obtained by the discrete Fourier transform (DFT), and the asterisk denotes the complex conjugate. We denote $S_n(f)$ as the one-sided noise power spectral density of LISA. The signal-to-noise ratio (SNR) of a GW signal can then be defined as $\rho = \sqrt{\langle h(f) | h(f) \rangle}$, while the normalized faithfulness reads

$$\mathcal{F}(h_a, h_b) = \frac{\langle h_a | h_b \rangle}{\sqrt{\langle h_a | h_a \rangle \langle h_b | h_b \rangle}}. \quad (4.18)$$

When $\mathcal{F} = 1$, the two GW signals are identical, and $\mathcal{F} = 0$ corresponds to a complete mismatch. In practice, it is customary to characterize deviations between waveforms in terms of the mismatch, defined as:

$$\mathcal{M}(h_a, h_b) = 1 - \mathcal{F}(h_a, h_b). \quad (4.19)$$

The mismatch provides a quantitative measure of distinguishability between two signals and serves as the primary diagnostic employed in our analysis.

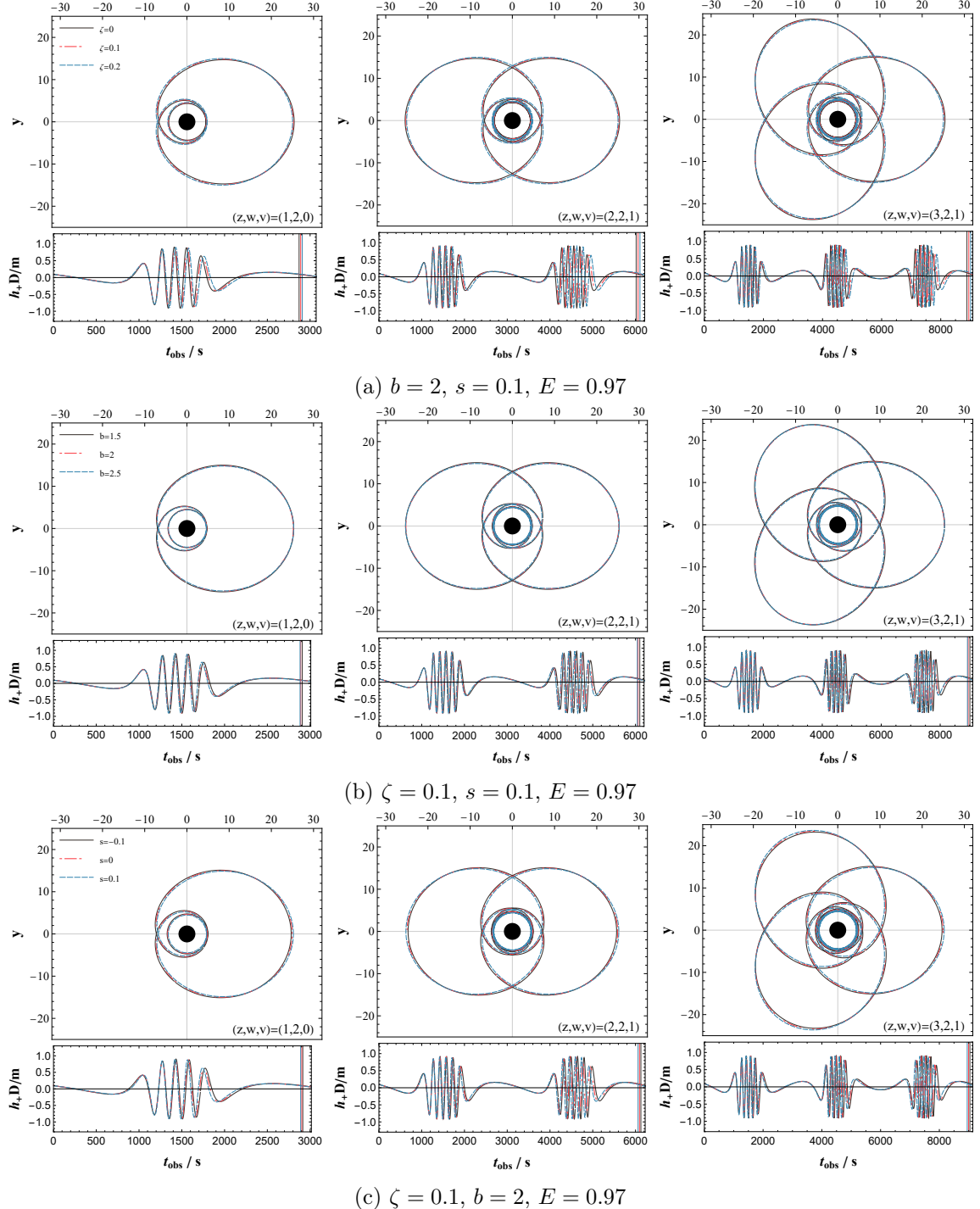
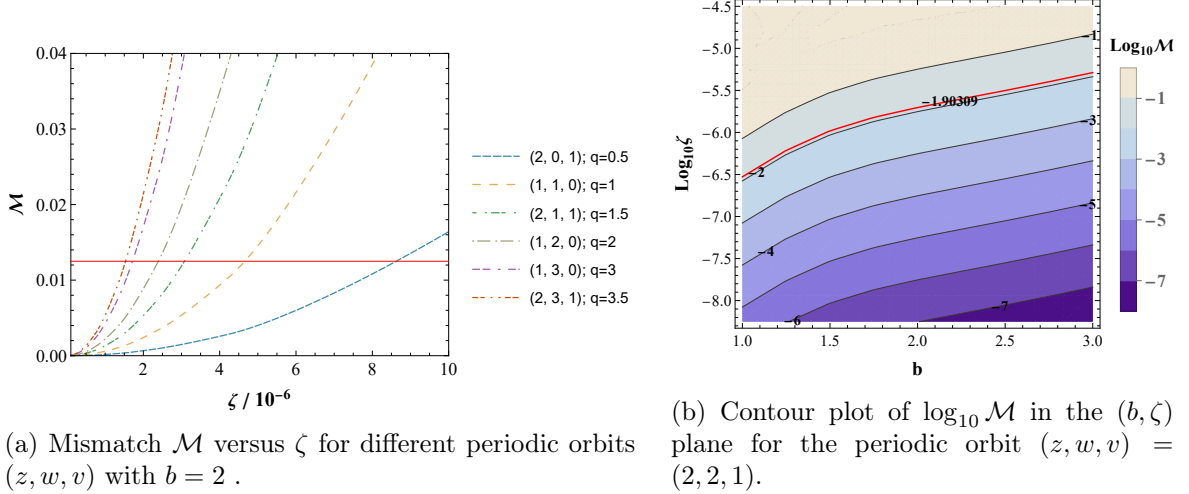


Figure 7: Periodic trajectories and the corresponding gravitational waveforms for different values of: (a) ζ , (b) b , and (c) spin s . The central black hole mass is set to $M = 10^6 M_\odot$, the compact object mass to $m = 10 M_\odot$, and the luminosity distance to $D = 10$ Gpc. Additionally, we adopt $\Theta = \pi/2$ and $\Phi = \pi/3$, which results in $h_x = 0$. The vertical line in the waveform marks the time corresponding to one complete orbital period.



(a) Mismatch \mathcal{M} versus ζ for different periodic orbits (z, w, v) with $b = 2$.

(b) Contour plot of $\log_{10} \mathcal{M}$ in the (b, ζ) plane for the periodic orbit $(z, w, v) = (2, 2, 1)$.

Figure 8: Mismatch in h_+ between gravitational waveforms from NLG black holes and Schwarzschild black holes after a one-year observation. We consider an EMRI system with the following parameters: $M = 10^6 M_\odot$, $m = 10 M_\odot$, $s = 0.1$ mM, $D = 1$ Gpc. Additionally, we adopt $\Theta = \Phi = \pi/2$. The red line corresponds to the mismatch $\mathcal{M} = 0.0125$.

4.3 Numerical results

In Fig. 7, we present three representative sets of periodic orbits together with their corresponding gravitational waveforms, illustrating the effect of the parameters: ζ , b , and the spin s . We note that variations in these parameters modify the orbital geometry. These changes, which appear primarily as shifts in the positions of perihelion and aphelion, are directly imprinted onto the emitted gravitational waveform.

In particular, relative to the Schwarzschild case an increase in ζ leads to a distinct phase delay in the waveform. The parameter b exerts a relatively weak influence on both the orbit and the waveform, yet our quantitative analysis reveals that increasing b results in a slight phase advance. Regarding the particle spin, when it is co-rotating, the waveform exhibits a phase advance, whereas a counter-rotating particle produces a phase delay—reflecting the modulation of orbital dynamics by spin-curvature coupling.

All the above analyses are conducted to elucidate the influence of parameters on gravitational waveforms, for which reason the parametric differences are intentionally set to be large—whereas in reality, such discrepancies may be extremely subtle. Consequently, the phase differences between these waveforms are small over a single orbital cycle, yet they accumulate over time due to minor variations in the orbital evolution rate. After a large number of orbital cycles, the accumulated phase shifts become significant enough to induce a statistically resolvable waveform mismatch in high signal-to-noise ratio observations. In other words, the long-term cumulative effect can amplify the impact of NLG on gravitational waveforms.

The mismatch between gravitational waveforms from Schwarzschild black holes and NLG black holes after one year of observation is presented in Fig. 8. We adopt a detectability threshold of $\mathcal{M} = 0.0125$, which means that when the mismatch exceeds this value, the two waveforms can be effectively distinguished.

Fig. 8a clearly shows that, for fixed $b = 2$, larger values of q correspond to smaller values of ζ required to reach the detectability threshold. This indicates that systems with higher q are more sensitive to NLG effects. In other words, more complex orbits provide greater

discrimination power for testing modified theories of gravity, consistent with the findings in [49].

Fig. 8b displays a contour plot of the mismatch \mathcal{M} in the (b, ζ) parameter plane. The region above the red curve (where $\mathcal{M} > 0.0125$) corresponds to the parameter regime for which GR and NLG waveforms are distinguishable. It is evident that, for a fixed ζ , increasing b reduces the mismatch, making it harder to differentiate between GR and NLG predictions. Consequently, longer observation times would be required to accumulate sufficient phase differences for detection.

5 Conclusion and discussion

This work presents a systematic analysis of the orbital dynamics of spinning particles and the corresponding GW signals in the static, spherically symmetric black hole solution derived from a modified DW NLG framework. The aim is to uncover the distinctive imprints of nonlocal gravitational corrections on spacetime structure. First, by employing the MPD equations together with the supplementary Tulczyjew spin condition, we derived the equations of motion for spinning particles in this NLG background. A timelike constraint was further imposed to eliminate unphysical superluminal trajectories.

We constructed an effective potential for radial motion and analyzed the permissible ranges of energy and angular momentum that support bound orbits. We computed key properties of the ISCO. Our results show that a larger nonlocal perturbation parameter ζ lowers the potential barrier and increases the ISCO radius, whereas a larger value of b raises the barrier and decreases the ISCO radius. Particle spin also modulates orbital stability: for spin aligned with the orbital angular momentum, the potential barrier is raised and the ISCO radius reduced; the opposite behavior is observed for anti-aligned spin, which manifests a distinct spin-orbit coupling effect.

Adopting the (z, w, v) classification scheme, we characterized the various kinds of periodic orbits and computed their associated gravitational waveforms. We found that nonlocal corrections induce measurable phase shifts in the waveforms: increasing ζ gives rise to phase delays, whereas increasing b causes phase advance. Similarly, co-rotating particles also produce phase advance. After a one-year observation, our calculations indicated that a value of $\zeta \sim 10^{-6}$ (for $b = 2$) produces a detectable waveform mismatch between NLG black holes and Schwarzschild black holes, while a larger value of b increases the difficulty of distinguishing NLG effects.

Future research directions can be extended to the study of black hole chaotic behavior. For instance, spinning particles may exhibit chaotic motion in black hole spacetimes [50–52]. Given that chaos is highly sensitive to the underlying spacetime geometry, diagnostic tools such as Lyapunov exponents and Poincaré sections can amplify subtle differences between NLG black holes and GR black holes, thereby offering a promising avenue for discriminating among different NLG theories.

Acknowledgments

This work is supported by the National Natural Science Foundation of China (NSFC) with Grant No. 12275087. MB is supported by Proyecto Interno UCM-IN-25202 línea regular.

References

- [1] SUPERNOVA SEARCH TEAM collaboration, *Observational evidence from supernovae for an accelerating universe and a cosmological constant*, *Astron. J.* **116** (1998) 1009 [[astro-ph/9805201](#)].
- [2] P.J.E. Peebles and B. Ratra, *The Cosmological Constant and Dark Energy*, *Rev. Mod. Phys.* **75** (2003) 559 [[astro-ph/0207347](#)].
- [3] J. Frieman, M. Turner and D. Huterer, *Dark Energy and the Accelerating Universe*, *Ann. Rev. Astron. Astrophys.* **46** (2008) 385 [[0803.0982](#)].
- [4] P. Brax, *What makes the Universe accelerate? A review on what dark energy could be and how to test it*, *Rept. Prog. Phys.* **81** (2018) 016902.
- [5] Y.B. Zel'dovich, A. Krasinski and Y.B. Zeldovich, *The Cosmological constant and the theory of elementary particles*, *Sov. Phys. Usp.* **11** (1968) 381.
- [6] S. Weinberg, *The Cosmological Constant Problem*, *Rev. Mod. Phys.* **61** (1989) 1.
- [7] S. Capozziello and F. Bajardi, *Nonlocal gravity cosmology: An overview*, *Int. J. Mod. Phys. D* **31** (2022) 2230009 [[2201.04512](#)].
- [8] S. Deser and R.P. Woodard, *Nonlocal Cosmology*, *Phys. Rev. Lett.* **99** (2007) 111301 [[0706.2151](#)].
- [9] S. Nojiri and S.D. Odintsov, *Modified non-local- $F(R)$ gravity as the key for the inflation and dark energy*, *Phys. Lett. B* **659** (2008) 821 [[0708.0924](#)].
- [10] S. Jhingan, S. Nojiri, S.D. Odintsov, M. Sami, I. Thongkool and S. Zerbini, *Phantom and non-phantom dark energy: The Cosmological relevance of non-locally corrected gravity*, *Phys. Lett. B* **663** (2008) 424 [[0803.2613](#)].
- [11] S. Capozziello, E. Elizalde, S. Nojiri and S.D. Odintsov, *Accelerating cosmologies from non-local higher-derivative gravity*, *Phys. Lett. B* **671** (2009) 193 [[0809.1535](#)].
- [12] S. Bahamonde, S. Capozziello and K.F. Dialektopoulos, *Constraining Generalized Non-local Cosmology from Noether Symmetries*, *Eur. Phys. J. C* **77** (2017) 722 [[1708.06310](#)].
- [13] E. Elizalde, S.D. Odintsov, E.O. Pozdeeva and S.Y. Vernov, *De Sitter and power-law solutions in non-local Gauss–Bonnet gravity*, *Int. J. Geom. Meth. Mod. Phys.* **15** (2018) 1850188 [[1805.10810](#)].
- [14] S. Deser and R.P. Woodard, *Nonlocal Cosmology II — Cosmic acceleration without fine tuning or dark energy*, *JCAP* **06** (2019) 034 [[1902.08075](#)].
- [15] F. Bajardi, S. Capozziello and D. Vernieri, *Non-local curvature and Gauss–Bonnet cosmologies by Noether symmetries*, *Eur. Phys. J. Plus* **135** (2020) 942 [[2011.01317](#)].
- [16] M. Maggiore and M. Mancarella, *Nonlocal gravity and dark energy*, *Phys. Rev. D* **90** (2014) 023005 [[1402.0448](#)].
- [17] T. Biswas, E. Gerwick, T. Koivisto and A. Mazumdar, *Towards singularity and ghost free theories of gravity*, *Phys. Rev. Lett.* **108** (2012) 031101 [[1110.5249](#)].
- [18] L. Modesto, *Super-renormalizable Quantum Gravity*, *Phys. Rev. D* **86** (2012) 044005 [[1107.2403](#)].
- [19] F. Brischese, A. Marcianò, L. Modesto and E.N. Saridakis, *Inflation in (Super-)renormalizable Gravity*, *Phys. Rev. D* **87** (2013) 083507 [[1212.3611](#)].
- [20] L. Modesto, *Super-renormalizable Gravity*, in *13th Marcel Grossmann Meeting on Recent Developments in Theoretical and Experimental General Relativity, Astrophysics, and Relativistic Field Theories*, pp. 1128–1130, 2015, DOI [[1302.6348](#)].

[21] T. Biswas, A.S. Koshelev and A. Mazumdar, *Consistent higher derivative gravitational theories with stable de Sitter and anti-de Sitter backgrounds*, *Phys. Rev. D* **95** (2017) 043533 [[1606.01250](#)].

[22] L. Buoninfante, A.S. Koshelev, G. Lambiase and A. Mazumdar, *Classical properties of non-local, ghost- and singularity-free gravity*, *JCAP* **09** (2018) 034 [[1802.00399](#)].

[23] E. Belgacem, A. Finke, A. Frassino and M. Maggiore, *Testing nonlocal gravity with Lunar Laser Ranging*, *JCAP* **02** (2019) 035 [[1812.11181](#)].

[24] C.-Y. Chen and S. Park, *Black hole quasinormal modes and isospectrality in Deser-Woodard nonlocal gravity*, *Phys. Rev. D* **103** (2021) 064029 [[2101.06600](#)].

[25] R. D'Agostino and V. De Falco, *Black hole solutions in the revised Deser-Woodard nonlocal theory of gravity*, *JCAP* **07** (2025) 046 [[2502.15460](#)].

[26] R. D'Agostino and V. De Falco, *Nonlocal gravity in a proper tetrad frame: traversable wormholes*, *JCAP* **05** (2025) 069 [[2501.18007](#)].

[27] R. D'Agostino and V. De Falco, *Quasinormal modes of nonlocal gravity black holes*, *Phys. Rev. D* **112** (2025) 064028 [[2507.01698](#)].

[28] LIGO SCIENTIFIC, VIRGO collaboration, *Observation of Gravitational Waves from a Binary Black Hole Merger*, *Phys. Rev. Lett.* **116** (2016) 061102 [[1602.03837](#)].

[29] LIGO SCIENTIFIC, VIRGO collaboration, *GWTC-1: A Gravitational-Wave Transient Catalog of Compact Binary Mergers Observed by LIGO and Virgo during the First and Second Observing Runs*, *Phys. Rev. X* **9** (2019) 031040 [[1811.12907](#)].

[30] LIGO SCIENTIFIC, VIRGO collaboration, *GWTC-2: Compact Binary Coalescences Observed by LIGO and Virgo During the First Half of the Third Observing Run*, *Phys. Rev. X* **11** (2021) 021053 [[2010.14527](#)].

[31] P.I. Jefremov, O.Y. Tsupko and G.S. Bisnovatyi-Kogan, *Innermost stable circular orbits of spinning test particles in Schwarzschild and Kerr space-times*, *Phys. Rev. D* **91** (2015) 124030 [[1503.07060](#)].

[32] Y.-P. Zhang, S.-W. Wei, W.-D. Guo, T.-T. Sui and Y.-X. Liu, *Innermost stable circular orbit of spinning particle in charged spinning black hole background*, *Phys. Rev. D* **97** (2018) 084056 [[1711.09361](#)].

[33] Y. Liu and X. Zhang, *Analytic solutions for the motion of spinning particles near braneworld black hole*, *Phys. Rev. D* **111** (2025) 044056 [[2408.06852](#)].

[34] Y. Du, Y. Liu and X. Zhang, *Spinning particle dynamics and the innermost stable circular orbit in covariant loop quantum gravity*, *JCAP* **05** (2025) 045 [[2411.13316](#)].

[35] S. Babak, J. Gair, A. Sesana, E. Barausse, C.F. Sopuerta, C.P.L. Berry et al., *Science with the space-based interferometer LISA. V: Extreme mass-ratio inspirals*, *Phys. Rev. D* **95** (2017) 103012 [[1703.09722](#)].

[36] Y. Liu and X. Zhang, *Gravitational waves for eccentric extreme mass ratio inspirals of self-dual spacetime*, *JCAP* **10** (2024) 056 [[2404.08454](#)].

[37] M. Mathisson, *Republication of: New mechanics of material systems*, *Gen. Rel. Grav.* **42** (2010) 1011.

[38] A. Papapetrou, *Spinning test particles in general relativity. 1.*, *Proc. Roy. Soc. Lond. A* **209** (1951) 248.

[39] W.G. Dixon, *A covariant multipole formalism for extended test bodies in general relativity*, *Nuovo Cim.* **34** (1964) 317.

[40] E. Harms, G. Lukes-Gerakopoulos, S. Bernuzzi and A. Nagar, *Spinning test body orbiting around a Schwarzschild black hole: Circular dynamics and gravitational-wave fluxes*, *Phys. Rev. D* **94** (2016) 104010 [[1609.00356](#)].

[41] M. Saijo, K.-i. Maeda, M. Shibata and Y. Mino, *Gravitational waves from a spinning particle plunging into a Kerr black hole*, *Phys. Rev. D* **58** (1998) 064005.

[42] J. Ehlers and E. Rudolph, *Dynamics of extended bodies in general relativity center-of-mass description and quasirigidity*, *Gen. Rel. Grav.* **8** (1977) 197.

[43] E. Hackmann, C. Lämmerzahl, Y.N. Obukhov, D. Puetzfeld and I. Schaffer, *Motion of spinning test bodies in Kerr spacetime*, *Phys. Rev. D* **90** (2014) 064035 [[1408.1773](#)].

[44] J. Levin and G. Perez-Giz, *A Periodic Table for Black Hole Orbits*, *Phys. Rev. D* **77** (2008) 103005 [[0802.0459](#)].

[45] J. Healy, J. Levin and D. Shoemaker, *Zoom-Whirl Orbits in Black Hole Binaries*, *Phys. Rev. Lett.* **103** (2009) 131101 [[0907.0671](#)].

[46] S. Babak, H. Fang, J.R. Gair, K. Glampedakis and S.A. Hughes, 'Kludge' gravitational waveforms for a test-body orbiting a Kerr black hole, *Phys. Rev. D* **75** (2007) 024005 [[gr-qc/0607007](#)].

[47] K. Glampedakis, *Extreme mass ratio inspirals: LISA's unique probe of black hole gravity*, *Class. Quant. Grav.* **22** (2005) S605 [[gr-qc/0509024](#)].

[48] E.E. Flanagan and S.A. Hughes, *Measuring gravitational waves from binary black hole coalescences: 1. Signal-to-noise for inspiral, merger, and ringdown*, *Phys. Rev. D* **57** (1998) 4535 [[gr-qc/9701039](#)].

[49] H. Gong, S. Long, X.-J. Wang, Z. Xia, J.-P. Wu and Q. Pan, *Gravitational waveforms from periodic orbits around a novel regular black hole*, [2509.23318](#).

[50] S. Suzuki and K.-i. Maeda, *Chaos in Schwarzschild space-time: The motion of a spinning particle*, *Phys. Rev. D* **55** (1997) 4848 [[gr-qc/9604020](#)].

[51] M.D. Hartl, *Dynamics of spinning test particles in Kerr space-time*, *Phys. Rev. D* **67** (2003) 024005 [[gr-qc/0210042](#)].

[52] O. Zelenka, G. Lukes-Gerakopoulos, V. Witzany and O. Kopáček, *Growth of resonances and chaos for a spinning test particle in the Schwarzschild background*, *Phys. Rev. D* **101** (2020) 024037 [[1911.00414](#)].